PAPER

Check for updates

Covalent Si–S bonding engineering in sulfurized polyacrylonitrile (SPAN): toward enhanced electrochemical stability and kinetics in lithium–sulfur batteries†

Qi Zhu,‡[a] Yi Gong,‡[b] Zongtao Zhang, [ID] *[a] Cheng Huang,[a] Miaoran Xu,[a] Kai Yang,*[b] Wei Zhang,[b] S. Ravi P. Silva [ID] *[b] and Yanfeng Gao [ID] *[c]

Sulfurized polyacrylonitrile (SPAN) is a promising cathode material for lithium–sulfur batteries due to its superior sulfur retention and long-term stability. However, the practical application of SPAN is hindered by insufficient sulfur anchoring sites and sluggish redox kinetics. Herein, we present an atomic-level bonding strategy to overcome these limitations by incorporating silicon quantum dots (SiQDs) into SPAN under high-temperature sulfurization (450 °C), forming robust covalent Si–S bonds with a high dissociation energy. These covalent Si–S bonds act as stable sulfur anchors, enabling a 19.77% higher sulfur loading with minimal free sulfur, while significantly improving electron/ion conductivity and redox reaction kinetics. The optimized $Si_{0.05}$-SPAN cathode exhibits outstanding electrochemical performance, including a high initial discharge capacity of 1432.7 mAh g^{-1} and a retained capacity of ~773 mAh g^{-1} after 500 cycles at 1.5 C, corresponding to an ultralow capacity decay of only 0.023% per cycle with nearly 100% coulombic efficiency. Comprehensive experimental characterization combined with density functional theory (DFT) calculations reveal that Si–S bonding redistributes electron density around sulfur atoms, effectively suppressing sulfur loss and accelerating charge transfer. This covalent bond engineering approach offers a new strategy for developing high-energy-density lithium–sulfur batteries with enhanced stability and kinetics.

Broader context

As global demand for high-performance, sustainable energy storage solution continues to grow, lithium–sulfur (Li–S) batteries have emerged as a leading candidate due to their exceptional theoretical capacity and natural abundance of sulfur. However, their commercialization is hindered by persistent challenges, most notably the polysulfide shuttle. One key strategy to address these problems is to covalently anchor sulfur within a stable host matrix, *e.g.*, sulfurized polyacrylonitrile (SPAN), to improve cycling reversibility. Yet, this approach is limited by low sulfur anchoring sites and sluggish redox kinetics. In this work, we introduce atomic-level integration of silicon into SPAN to form a robust covalent Si–S bonding network through high-temperature sulfurization. These bonds, which exhibit superior thermodynamic stability compared to conventional weak sulfur interactions, effectively stabilize sulfur and suppress polysulfide dissolution in an ether electrolyte. Simultaneously, they accelerate redox kinetics, thereby enabling higher sulfur utilization. This molecular anchoring strategy not only resolves long-standing degradation mechanisms but also redefines the design principles for sulfur hosts, by combining high capacity with long-term stability. Practically, the improvements in sulfur retention and reaction kinetics represent critical advancements toward realizing Li–S batteries with the cycle life and energy density required for electric vehicles and grid-scale storage.

[a]*School of Materials Science and Engineering, Zhengzhou University, Kexue Ave 100, Zhengzhou 450001, China. E-mail: ztzhang@zzu.edu.cn*
[b]*Advanced Technology Institute, University of Surrey, Guildford, Surrey GU2 7XH, UK. E-mail: kai.yang@surrey.ac.uk, s.silva@surrey.ac.uk*
[c]*School of Materials Science and Engineering, Shanghai University, Shangda Rd 99, Shanghai 200444, China. E-mail: yfgao@shu.edu.cn*

‡These authors contributed equally to this work.

1 Introduction

Developing sustainable, high-efficiency energy storage systems with high energy density, long cycle life, and low cost is a critical global challenge.[1–3] Among emerging battery technologies, lithium–sulfur (Li–S) batteries are one of the most promising candidates, due to sulfur's exceptionally high theoretical capacity (1675 mAh g^{-1}), Earth abundance, and environmental compatibility.[4–9] However, the practical deployment of Li–S

batteries is impeded by several major issues, including the notorious shuttle effect caused by the dissolution and migration of lithium polysulfides (LiPSs), the substantial volume expansion of sulfur during lithiation, and inherently sluggish sulfur redox kinetics, all of which lead to rapid capacity fading.[10]

One of the most promising cathode solutions to mitigate these issues is sulfurized polyacrylonitrile (SPAN), which co-valently traps sulfur within a carbon–nitrogen polymer matrix.[11] In SPAN, the sulfur is bound in a short-chain form, preventing the formation of long-chain LiPSs and largely elimi-nating the shuttle effect in carbonate electrolytes.[12,13] However, in the ether-based electrolyte typically used with lithium metal anodes, even these short-chain Li_2S_n ($n \leq 4$) species are soluble, leading to polysulfide dissolution and con-tinued shuttling. In addition, the widespread adoption of SPAN cathodes is still constrained by other challenges, such as poor conductivity, sluggish solid-state conversion kinetics, and limited sulfur loading content (typically 30–45 wt% at 350–400 °C processing) due to limited anchoring sites in the PAN framework. Attempts to simply add more sulfur often produce unbound free S_8 that causes capacity decay, while higher sulfurization temperatures (>450 °C) promote PAN cyclization and graphitization (improving the conductivity and structural stability) but drastically reduce the retained sulfur content.[14,15]

Chemical bonding engineering has recently emerged as an effective strategy to improve the performance of SPAN cath-odes. For example, selenium doping of SPAN can stabilize the bound sulfur through Se–S bonds, achieving ultra-stable cycling of over 800 cycles with only 0.029% decay per cycle.[16–18] Additionally, coordinating SPAN with transition-metal sites, e.g., Co–N_4S, has been shown to enhance elec-tronic conductivity to ∼0.17 S cm^{-1} and provide extra polysul-fide binding sites. These advances highlight the critical impor-tance of developing new chemical bonding approaches to maximize sulfur utilization while improving electrochemical performance.[19–23] However, Se doping is hindered by high material costs and the formation of irreversible Li_2Se side reac-tions, while metal modification also suffers from metal leach-ing and reduced energy density. In this context, silicon (Si), a chemically versatile element, provides an elegant elemental solution positioned adjacent to the sulfur group in the element periodic table. Notably, silicon can form a covalent Si–S bond with a high dissociation energy (∼147 kJ mol^{-1}), which is significantly higher than those of commonly reported bonding systems, such as S–Te (60 kJ mol^{-1}), S–N (115 kJ mol^{-1}), S–Sb (70.6 kJ mol^{-1}) and S–S (101.5 kJ mol^{-1}).[24–26] Moreover, the conductivity of silicon (≈10^{-3} S cm^{-1}) is several orders of magnitude larger than that of sulfur, which could help address the charge-transfer limitations of SPAN. Despite these potentials, integrating Si–S chemistry into SPAN architec-tures has proven challenging, primarily due to critical bottlenecks of high synthesis temperature required for bond formation and silicon aggregation during thermal processing.[27,28]

Herein, we report the first successful integration of covalent Si–S bonds into SPAN cathodes by in situ reacting silicon quantum dots (SiQDs) with PAN during high-temperature sul-furization. By optimizing the sulfurization temperature and SiQD doping level, we achieved a record sulfur content of 37.93 wt% in the SPAN composite when annealed at 450 °C (22.6% higher than that of the undoped sample), while main-taining minimal free sulfur. The SiQD-engineered SPAN cathode delivers exceptional performance, with an initial dis-charge capacity of 1432.7 mAh g^{-1} at 0.1 C and a retention capacity of 773.2 mAh g^{-1} after 500 cycles at 1.5 C, corres-ponding to an ultralow decay rate of 0.023% per cycle. Spectroscopic analysis combined with DFT modeling indicates that the introduced Si–S bonds redistribute electron density around sulfur atoms, which mitigates sulfur loss and opti-mizes charge transfer pathways during cycling. This work demonstrates an effective atomic-level bond engineering strat-egy for Li–S batteries, establishing a robust platform that bridges fundamental materials innovation with practical battery applications.

2 Experimental

2.1 Materials

3-Aminopropyltriethoxysilane (APTES, 97 wt%) was purchased from Usolf Chemical Technology Co. Ltd, Shandong, and used as the silicon source. PAN (M_w = 150 000 g mol^{-1}) is purchased from Sigma Aldrich Trading Co. Ltd, Shanghai. Sublimation sulfur (S, ≥99.5 wt%) and anhydrous glucose (AR, 99 wt%) are purchased from Komeo Chemical Reagent Co. Ltd, Tianjin. N,N-Dimethylformamide (DMF) and acetonitrile (AR, ≥99.5 wt%) were purchased from Sinopharm Chemical Reagent Co. Ltd, China. Polyvinylpyrrolidone (PVP) (M_w = 58 000 g mol^{-1}) was purchased from Aladdin Biochemical Technology Co. Ltd, Shanghai. CNTs with a diameter of 8–15 nm and length of 10–50 μm were purchased from Chengdu Organic Chemicals Co. Ltd, China. 1,3-Dioxolane (DOL), 1,2-dimethoxyethane (DME) and lithium bis(trifluoro-methanesulfonyl) imide (LiTFSI) were brought from Alfa Aesar. All chemicals and solvents were analytical grade and used without further purification.

2.2 Materials synthesis

2.2.1 Synthesis of SiQDs. 1 mL APTES is mixed with 4 mL of deionized water under vigorous stirring for 10 min to ensure that APTES is fully hydrolyzed. Then, 1 mL glucose aqueous solution (0.24 M) is added and mixed in a water bath at 70 °C for 20 min. After that, acetonitrile solution (the volume ratio of SiQD solution/acetonitrile is fixed at 1 : 4) is added to remove the impurities in the reaction product. The obtained precipitates are centrifuged and washed to get the final SiQD powders.[29]

2.2.2 Preparation of SPAN and Si$_x$-SPAN cathode materials. Appropriate amounts of the as-obtained SiQDs are added into DMF and mixed with CNT, PAN, PVP, and sublimed sulfur

(weight ratio of 1 : 4 : 4 : 16) in a water bath at 60 °C for 12 h. The addition amounts of SiQDs vary by 2.5 wt%, 5.0 wt%, and 10.0 wt%, respectively. The obtained mixed solution is barcoated onto a PET substrate, which is immediately immersed in deionized water and ultrasonically treated for about 1 h. After that, the obtained precursor membranes are dried under vacuum at 60 °C overnight under an Ar atmosphere. The obtained samples are further annealed in a tube furnace at elevated temperatures above 450 °C for 6 h to obtain the SiQD doped SPAN electrodes. A pure SPAN sample is also synthesized without the addition of SiQDs. The doped electrodes are denoted as $Si_{0.025}$-SPAN, $Si_{0.05}$-SPAN, and $Si_{0.1}$-SPAN, respectively, for samples with 2.5%, 5%, and 10% SiQD doping content.

2.3 Materials characterization

The morphologies of Si_x-SPAN are characterized by scanning electron microscopy (SEM, Auriga FIB, Zeiss, Germany). Transmission electron microscopy (TEM, FEI, Tecnai G2 F20, USA) is used to characterize the structures and morphologies of the Si_x-SPAN samples. X-ray photoelectron spectroscopy (XPS) spectrum is analyzed on a PHI Quantera SXM (ULVAC-PHI, Kanagawa, Japan) system with an Al/K anode (photon energy = 1486.6 eV) mono X-ray source. X-ray diffraction (XRD) is performed on an X-ray diffractometer (DX-2700BH, Dandong Haoyuan Ltd, Liaoning, China) using Cu Kα as the radiation source. Raman spectroscopy is performed using a Confotec MR520 instrument (Graben, Germany) with an excitation wavelength of 532 nm. Fourier transform infrared (FTIR) spectra are recorded using a Bruker Vertex 70 FTIR spectrometer. Thermogravimetric (TG) analysis is performed under nitrogen flow using a thermal analyzer (STA449F3, NETZSCH, Germany) at a heating rate of 10 °C min^{-1} from room temperature to 1000 °C. Nitrogen adsorption–desorption isotherms are recorded using an ASAP 2460 (Micromeritics Shanghai, China) at a temperature of 77 K. The specific surface area and the pore structure are measured by nitrogen sorption using a physisorption analyzer (JW-BK112, Beijing, China). CP/MAS (cross-polarized magic angle spinning) NMR spectra are obtained on a 14.1 T wide-bore Bruker Avance III (Germany) spectrometer with a 4 mm dual-resonance magic angle rotating probe tip. The Larmor frequencies of ^{13}C and ^{29}Si are 150.92 and 119.24 MHz, respectively.

2.4 Electrochemical measurements

The obtained flexible SPAN and Si_x-SPAN composites are used directly as the cathode and lithium metal foil as the anode to assemble the CR2032 coin cells. The ether-based electrolyte is made of 1 M lithium bis(trifluoromethanesulfonyl)imide (LiTFSI) and 0.1 M $LiNO_3$ dissolved in 1,3-dioxolane (DOL) and 1,2-dimethoxyethane (DME) solution (1 : 1, v/v). The amount of electrolyte in the cells is 40 μL, and the electrolyte to sulfur (E/S) ratio is approximately 8 μL mg^{-1}. The electrode had an active material loading of 1.5 mg cm^{-2}, a diameter of 12 mm, and a thickness of approximately 400 μm. Galvanostatic charge/discharge (GCD) and rate performances are measured on a battery test system (LANDCT2001A, Wuhan Electronics Co., Ltd Wuhan, China) with cycling voltages ranging from 1.0 to 3.0 V with different cycle rates. Cyclic voltammetry (CV) with various scan rates and electrochemical impedance spectroscopy (EIS, 10 mHz to 100 kHz) measurements are carried out with an AUTOLAB electrochemical instrument (PGSTAT302N, Metrohm, Switzerland). Specific charge/discharge capacities are calculated based on the mass of sulfur in SPAN and Si_x-SPAN.

2.5 DFT calculations

The density functional theory (DFT) calculations in this study are carried out using the Vienna *Ab Initio* Simulation Package (VASP). Evaluation of the exchange-correlation energy is performed using the Generalized Gradient Approximation (GGA) coupled with the Perdew–Burke–Ernzerhof (PBE) function. The electron–ion interactions are described through the Projector Augmented Wave (PAW) method. The plane wave expansion energy cutoff is established at 500 eV. Convergence criteria are set at 10^{-5} eV for energy and 0.02 eV $Å^{-1}$ for force. In slab model computations, a 15 Å vacuum spacing is introduced to mitigate the interactions between periodic images. Furthermore, for these models, dipolar correction is applied with the symmetrization disabled. The *K*-point setting is adjusted to 2 × 2 × 1 and spin polarization is included in all calculations.

3 Results and discussion

The schematic diagram of the synthesis process for the Si_x-SPAN composite electrode is illustrated in Fig. 1(a). Briefly, SiQD particles are synthesized by directly reducing 3-aminopropyltriethoxysilane (APTES) with glucose.[29] These SiQDs are then mixed with S, PAN, PVP and CNTs in DMF solution, followed by bar-coating onto the PET substrates to form a precursor membrane. The precursor membrane is subsequently immersed in deionized water, causing rapid phase separation that forms solvent/nonsolvent domains within the membrane.[30] After thermal treatment at 450 °C under the Ar atmosphere, flexible SiQD doped hierarchically porous SPAN (or Si_x-SPAN) electrodes are obtained. As shown in Fig. 1(e and f) and Fig S1,† the Si_x-SPAN electrodes are mechanically robust and can withstand repeated bending.

The high-resolution transmission electron microscopy (HR-TEM) image (Fig. 1b) reveals that the synthesized SiQDs are uniformly dispersed with a particle size of 3–5 nm. Scanning electron microscopy (SEM) and HRTEM images further confirm the hierarchically porous structures with CNT networks embedded throughout the electrodes (Fig. S1 and S2†), which can enhance efficient ion and electron transport. Notably, after the sulfurization step at 450 °C, no independent SiQDs or aggregated Si particles are observed, suggesting that the SiQDs react with the PAN/sulfur precursor during annealing. Energy dispersive X-ray spectroscopy (EDS) elemental mapping (Fig. 1h–k) further shows that Si is homogeneously
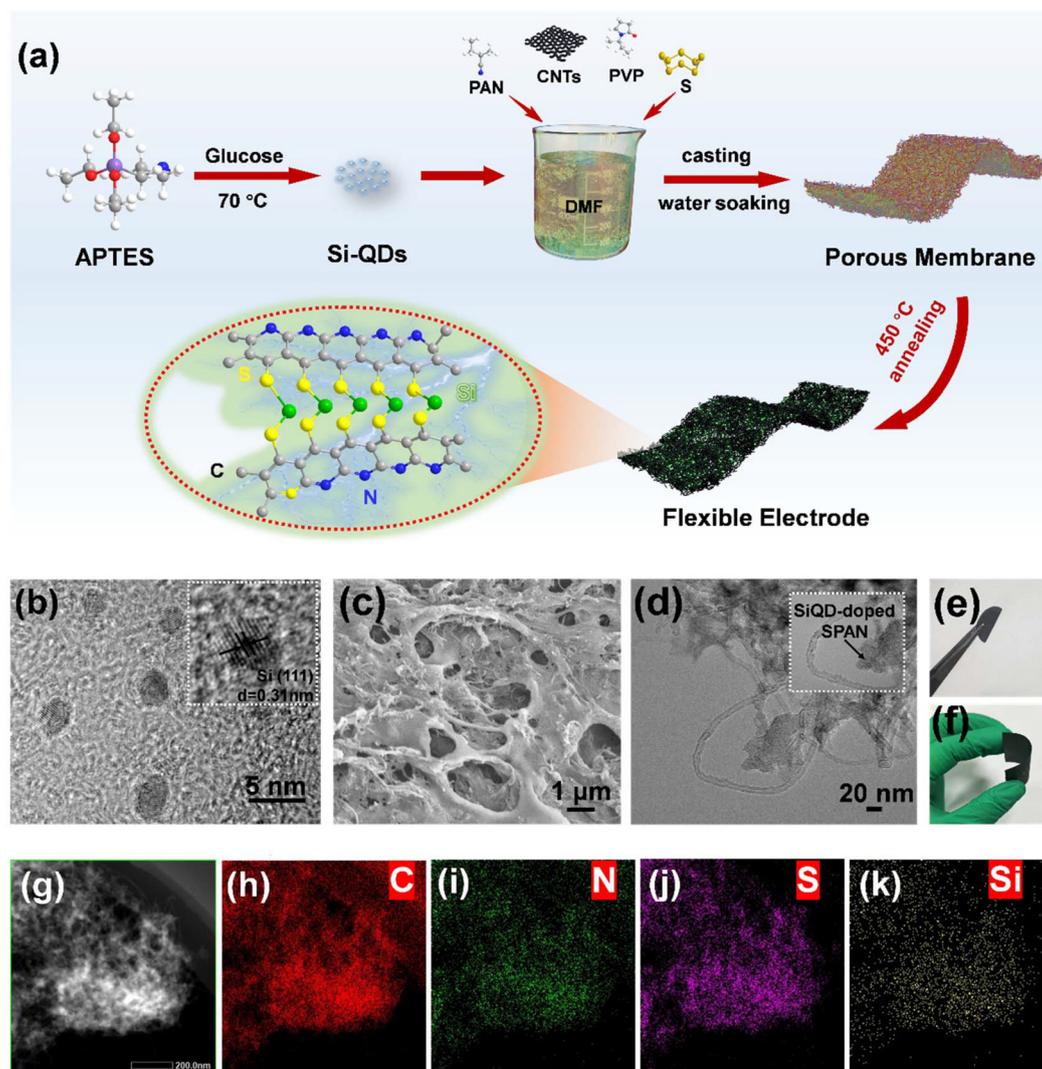
Fig. 1 (a) Schematic diagram of the synthesis and structural evolution of the composite electrodes. (b)–(d) SEM and TEM images of the Si$_{0.05}$-SPAN composite electrode. (e and f) The mechanical test of the Si$_{0.05}$-SPAN composite electrode under different bending conditions. TEM dark field image (g) and the corresponding EDS elemental mappings of C, N, S and Si signals (h–k) for the Si$_{0.05}$-SPAN sample.

distributed alongside C, N, and S in the SPAN matrix, indicating successful incorporation of Si into the SPAN framework.

The structure and composition of the Si$_x$-SPAN composites are further analyzed by X-ray diffraction (XRD), Raman spectroscopy and Fourier transform infrared (FT-IR) spectroscopy, as shown in Fig. 2(a)–(c). XRD results show the expected orthorhombic phase (S$_8$, JCPDS card no.: 08-0247) and PAN exhibits a characteristic (110) diffraction at $2\theta = 17°$. After annealing the PAN–sulfur mixtures (SPAN formation) in N$_2$, a broad diffraction peak at 22° to 25° appears, corresponding to the (002) graphitic plane of SPAN produced by pyrolysis and cyclic reactions.[31] The XRD pattern of the Si$_x$-SPAN composite closely resembles that of the undoped SPAN (Fig. S3†), indicating that the overall SPAN structure is retained upon SiQD addition. No distinct diffraction patterns for crystalline Si (as shown in the green line in Fig. 2(a))[32] are observed in the Si$_x$-SPAN, consist-

ent with the low Si content and the amorphous nature of Si in the composite.

Fig. 2(b) and (c) present the FTIR results of the SPAN and Si$_{0.05}$-SPAN samples. FTIR spectra of both SPAN and Si$_{0.05}$-SPAN display strong absorption bands at 1497 cm^{-1} and 1222 cm^{-1}, corresponding to the stretching vibrations of C=C and C=N in the conjugated PAN backbone, and a band at 801 cm^{-1} attributed to the breathing mode of aromatic rings.[29,31,32] Table S1† summarizes the detailed peak assignments.[33] A notable difference in the Si$_{0.05}$-SPAN FTIR spectrum is observed in the 460–520 cm^{-1} region, where the multiple S–S absorption peaks present in SPAN are significantly shifted, and a new Si–S absorption peak appears at 488 cm^{-1}.[34,35] This new absorption is characteristic of Si–S bond formation, indicating that covalent Si–S bonding is introduced in the SiQD doped sample. The other Si$_x$-SPAN samples (2.5% and 10% Si,
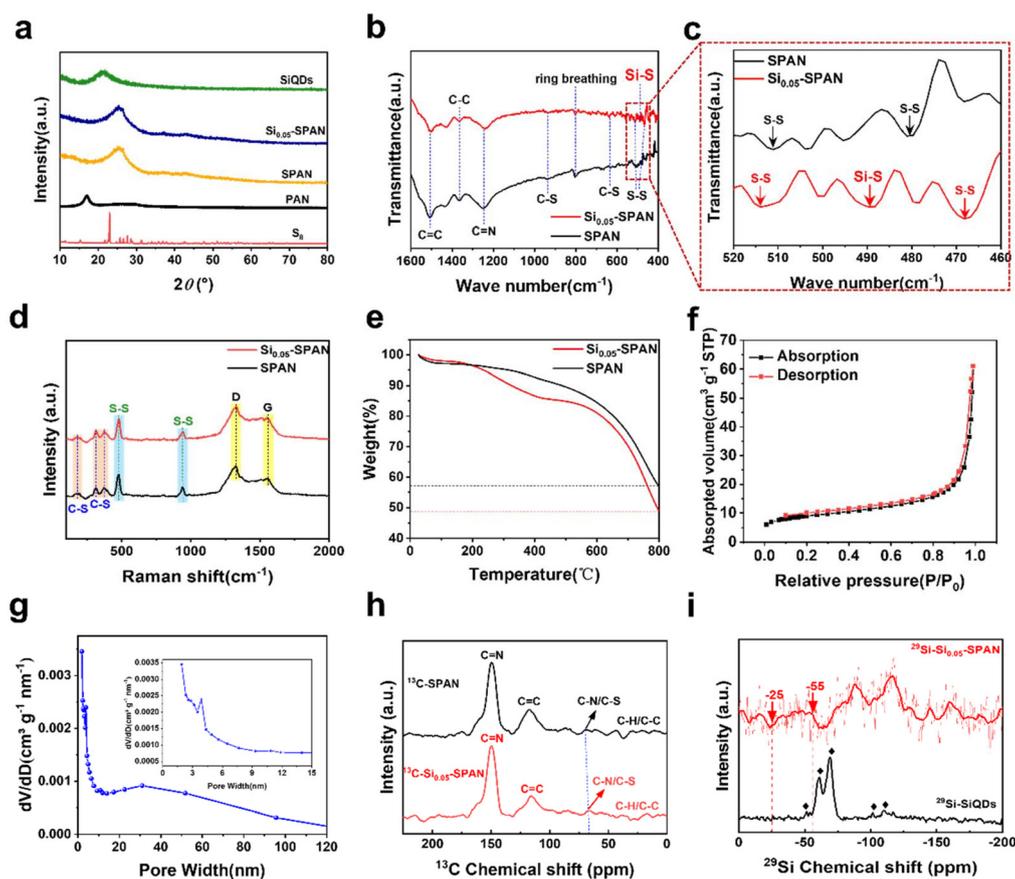
Fig. 2 (a) XRD patterns of the $Si_{0.05}$-SPAN, SiQDs, SPAN, PAN and S, respectively. (b and c) Fourier transform infrared (FTIR) and (d) Raman spectra of the $Si_{0.05}$-SPAN and SPAN samples. (e) Thermogravimetric (TG) analysis of $Si_{0.05}$-SPAN and SPAN; (f) N_2 adsorption–desorption curves and the corresponding pore size distribution (the inset in (f) and (g) of the $Si_{0.05}$-SPAN sample obtained by the Brunauer–Emmett–Teller (BET) method). (h) ^{13}C and (i) ^{29}Si CP-MAS NMR spectra of SPAN and $Si_{0.05}$-SPAN.

Fig. S4†) show similar features. A summary of peak assignments is given in Table S2.†[36,37] Raman spectra (Fig. 2d) provide additional evidence of the structural changes. Both SPAN and $Si_{0.05}$-SPAN exhibit Raman modes at 173, 312 and 371 cm^{-1}, corresponding to the C–S vibrations in SPAN,[31] and modes at 482 and 943 cm^{-1} correspond to the stretching vibration of the S–S bond. The disordered D band and graphite G band of carbon appear at 1325 cm^{-1} and 1550 cm^{-1}, respectively.[14] Notably, the intensity ratio I_G/I_D increases from 0.86 in SPAN to 0.98 for $Si_{0.05}$-SPAN, suggesting a higher degree of graphitization in the Si doped sample. Additionally, the I_G/I_D ratio increases significantly with higher annealing temperatures (Fig. S5†), consistent with improved electron transport properties under high-temperature annealing.[38–40] The absence of characteristic Raman modes for Si–S bonds, such as those at 448 cm^{-1},[41,42] is expected due to the low Si amount.

Thermogravimetric analysis (TGA) curves measured under an Ar atmosphere (Fig. 2e and S6†) show a slight weight loss below ~130 °C followed by a major weight loss at ~500 °C, corresponding to the evaporation of free water and the release of sulfur and other residuals (N or H atoms) during SPAN formation. The $Si_{0.05}$-SPAN sample shows a similar thermal

profile but with a larger total mass loss, indicating a higher sulfur content. Such a high sulfur content at this elevated processing temperature is unusual. Typically, PAN sulfurization at 300–350 °C yields 30% to 45% sulfur, but this drops to 25%–35% at 380–400 °C and around 20% at 450 °C due to the volatilization of sulfur. In our SiQD doped system, the strong Si–S bonding likely stabilizes more sulfur during the high temperature annealing, counteracting the tendency for sulfur loss. Fig. 2f and g present the Brunauer–Emmett–Teller (BET) results for the $Si_{0.05}$-SPAN composite. The N_2 adsorption–desorption isotherm shows a type IV curve with a clear hysteresis loop, indicating a hierarchically porous structure with micropores (<2 nm), meso-pores (2–50 nm) and large nano-/macropores (>50 nm). Such multiscale porosity is advantageous for Li–S cathodes because it increases the electrolyte-accessible reactive surface areas and thus enhances reaction kinetics and cycling stability.[43] The specific surface area of $Si_{0.05}$-SPAN is about 32.3 m^2 g^{-1} higher than that of undoped SPAN (24.6 m^2 g^{-1}) and significantly higher than the surface area of ~12.9 m^2 g^{-1} obtained using conventional annealing at 450 °C.

In addition, we analyzed the chemical structures of SPAN, SiQDs and $Si_{0.05}$-SPAN using ^{13}C and ^{29}Si cross-polarized

magic angle spinning (CP-MAS) NMR spectra (Fig. 2g and h). The ^{13}C NMR spectra of SPAN and $Si_{0.05}$-SPAN show prominent characteristic signals at 150 ppm and 117 ppm, corresponding to sp^2-hybridized carbons of C=N and C=C environments, respectively, confirming the presence of conjugated heterocyclic structures in both samples.[44] The signals at 70 ppm and 66 ppm are attributed to carbon atoms bonded to electron-withdrawing elements (such as sulfur and nitrogen). Notably, the relative intensity of signals in the 10–40 ppm and 110–140 ppm regions[44] is reduced in SPAN and $Si_{0.05}$-SPAN compared to that of pure PAN, indicating extensive cyclization and the formation of conjugated heterocyclic structures upon sulfurization. In the ^{29}Si CP-MAS NMR spectra of $Si_{0.05}$-SPAN, the characteristic chemical shift for crystalline Si ($\sim$−80 ppm) is nearly absent, replaced by a broad peak in the range of amorphous Si ($\sim$−50 ppm), indicating the breakdown of crystalline Si structures. The two chemical shifts at −25 ppm and −55 ppm are assigned to the Si–S bonding,[45,46] suggesting that silicon coordinates with sulfur atoms. Additionally, the chemical shifts at −101 ppm and −110 ppm suggest the presence of Si–O bonds, likely from partial surface oxidation of SiQDs or Si atoms bonded to residual oxygen functionalities.[47–49] These NMR results corroborate that in the $Si_{0.05}$-SPAN composite, silicon exists in largely amorphous, chemically bonded forms rather than as crystalline silicon, consistent with the XRD observations.

To further explore the chemical structure of the Si_x-SPAN composites, we conducted X-ray photoelectron spectra (XPS) measurements. Fig. 3 presents the XPS results of the $Si_{0.05}$-SPAN composites. The XPS survey spectrum confirms the presence of C, N, O, S, and Si in the composites. The high-resolution C 1s spectrum shows four peaks at 284.8 eV, 285.5 eV, 286.7 eV, and 289.1 eV, corresponding to C–C/C=C, C–S, C–N,

and S–C≡N bonds, respectively, which align with the C–S bonds and pyridine N structures in SPAN.[50,51] Generally, the presence of pyridine N is known to enhance the electronic/ionic conductivity and provide additional adsorption sites for lithium polysulfide in Li–S systems.[44,52] The S 2p spectra centered at 164.6 eV (S 2p3/2) and 165.7 eV (S 2p1/2) are attributed to the C–S_x–C bonds, while the peaks at 162.2 eV (S 2p3/2) and 163.5 eV (S 2p1/2) are assigned to the Si–S–C formation after SiQD incorporation.[53–55] A minor set of XPS peaks at 168.3 eV and 169.6 eV is also present, which can be attributed to the –SO_x– bonds from oxidized sulfur species.[31,56] Importantly, the S 2p peaks in $Si_{0.05}$-SPAN are shifted by 0.4 eV towards higher binding energies compared to those in undoped SPAN (Fig. 3e, f, and Fig. S7†), indicating a change in the electronic environment of sulfur due to the strong electronic interactions between S and Si. The Si 2p spectrum displays a double peak at 103.6 eV and 104.1 eV, characteristic of Si–S bonds.[57–61] The absence of Si–Si bond peaks, together with the presence of the Si–S peak and the shift in S 2p binding energies, confirms that silicon is predominantly incorporated by forming covalent Si–S bonds within the SPAN network.

To evaluate the benefits of SiQD incorporation, we compare the electrochemical performance of SPAN and Si_x-SPAN cathodes with varying SiQD contents. As shown in Fig. 4a, 5 wt% of SiQDs is the optimal amount for achieving the highest electrochemical properties. Notably, the $Si_{0.05}$-SPAN electrode delivers high specific capacities of 1432.7, 1340.8, 1027.7, 705.1, and 482.5 mAh g^{-1} at 0.1 C, 0.2 C, 0.5 C, 1 C, and 2 C (1 C = 1675 mAh g^{-1}), respectively. The discharge capacity recovered to 1319.8 mAh g^{-1} when the current was switched back to 0.1 C, demonstrating excellent cycling stability. Insufficient SiQDs may not provide enough Si–S bonding to fully stabilize the S, while excessive incorporation could introduce too many
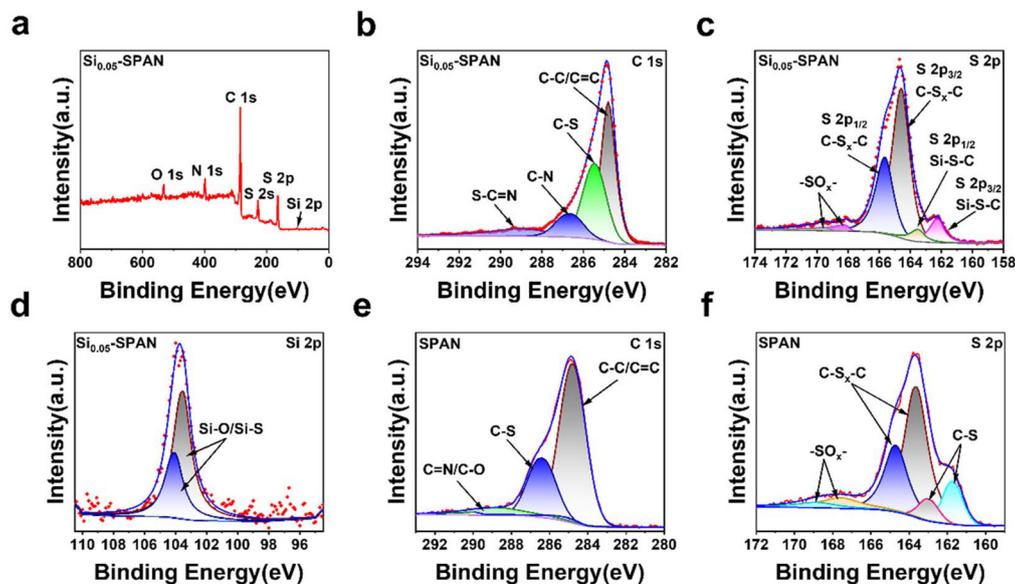

Fig. 3 (a) XPS survey spectra of the $Si_{0.05}$-SPAN sample. The elements Si, S, C, N and O are found in the sample; high-resolution XPS spectra of carbon (b), S 2p (c) and Si 2p (d) in $Si_{0.05}$-SPAN; and (c) high-resolution XPS of carbon (e) and S 2p (f) in SPAN.

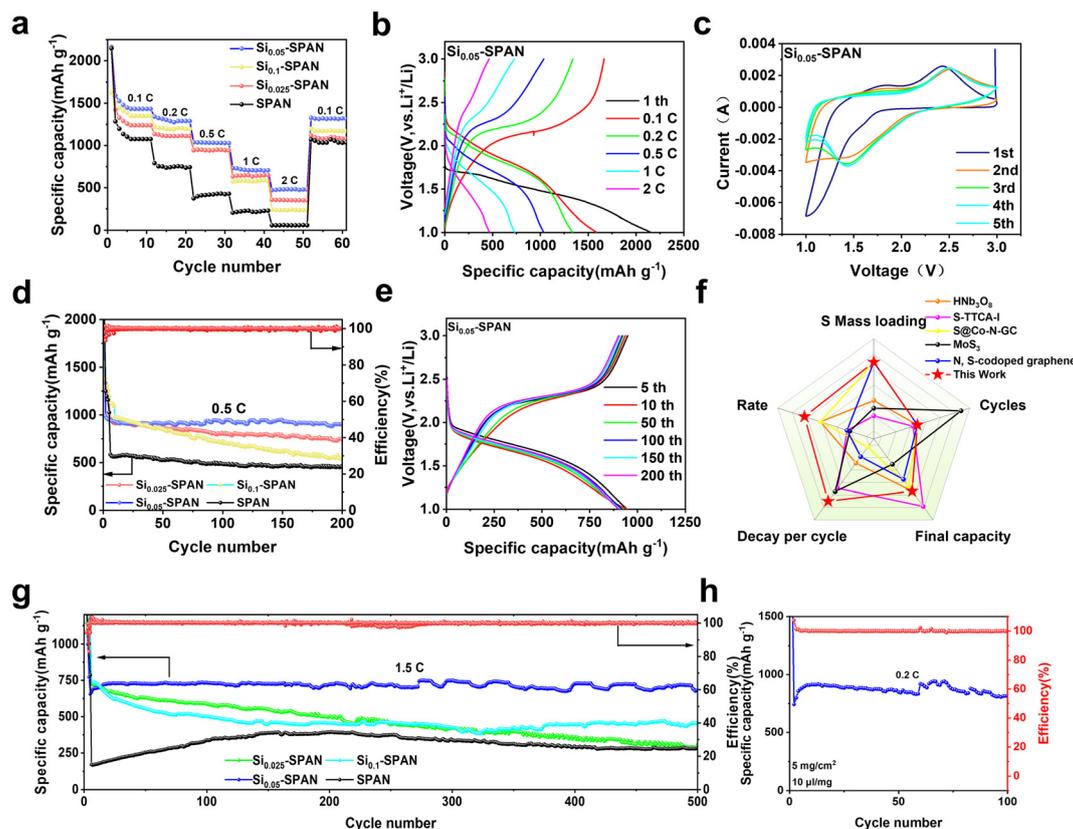**Fig. 4** (a) Rate performance of samples of $Si_{0.025}$-SPAN, $Si_{0.05}$-SPAN, $Si_{0.1}$-SPAN and SPAN, respectively. (b) The charge–discharge profiles of the $Si_{0.05}$-SPAN cathode cell, measured at 0.1 to 2 C. (c) CV curves of the first five cycles at a scan rate of 0.5 mV s^{-1} for the $Si_{0.05}$-SPAN cathode sample. (d) Cycling performance of $Si_{0.025}$-SPAN, $Si_{0.05}$-SPAN, $Si_{0.1}$-SPAN and SPAN cathode cells at 0.5 C. (e) Charge–discharge profiles of $Si_{0.05}$-SPAN at 0.5 C. (f) Radar charts for a comparison of the obtained $Si_{0.05}$-SPAN cathode with those in other literature reports (ref. 64–68). (g) Cycling performance of the $Si_{0.025}$-SPAN, $Si_{0.05}$-SPAN, $Si_{0.1}$-SPAN and SPAN cathodes at 1.5 C. (h) Cycling performance of $Si_{0.05}$-SPAN electrodes with high sulfur loading at 0.2 C.

insulating sites or disrupt conductivity. These results confirm that a moderate level of SiQD doping (around 5 wt%) is ideal for maximizing capacity and rate capability. For comparison, we summarize in Table S4 (in the ESI†) the performances of various SPAN-based cathodes reported in the literature. The $Si_{0.05}$-SPAN developed shows one of the highest capacities and best rate performances among reported SPAN cathodes, highlighting the effectiveness of the Si–S bond engineering strategy.

Moreover, the charge–discharge curves of $Si_{0.05}$-SPAN (Fig. 4b) show a sloping voltage plateau at 1.5 V, which increases to 1.7 V from the second cycle without the appearance of dissolved polysulfides. This is further supported by the cyclic voltammetry (CV) curves of $Si_{0.05}$-SPAN composites. As shown in Fig. 4(c) and S8,† during the anodic scan, only a single oxidation peak at ~2.3 V is observed, which is consistent with the cycling profiles of non-long-chained Li_2S_n species during cycling.[62,63]

Fig. 4d presents the cycling results at a discharge rate of 0.5 C. Following four activation cycles at 0.1 C, the initial discharge capacities of $Si_{0.025}$-SPAN, $Si_{0.05}$-SPAN, $Si_{0.1}$-SPAN and SPAN are 943.4, 950.6, 980.9 and 585.9 mAh g^{-1}, respectively. After 200 cycles, the $Si_{0.05}$-SPAN electrode retains the highest

discharge capacity of 902.2 mAh g^{-1}, with a low capacity decay rate of only 0.025% per cycle. In contrast, $Si_{0.025}$-SPAN, $Si_{0.1}$-SPAN and SPAN exhibit capacities of 741.9, 546.5 and 454.7 mAh g^{-1} after 200 cycles, with decay rates of 0.106%, 0.221%, and 0.112% per cycle, respectively. The electrochemical performance of electrodes with a high silicon quantum dot content declines primarily due to the aggregation of silicon and the degradation of the system's electrical properties, specifically impedance, caused by the excessive silicon introduction. The charge–discharge curves of $Si_{0.05}$-SPAN are also analyzed over extended cycling (Fig. 4e). The highly overlapping curves from the 5th to the 200th cycle indicate excellent electrochemical stability and improved reaction kinetics after SiQD doping. Most noticeably, the Si_x-SPAN cathodes demonstrate superior electrochemical performance compared to those in the literature reports, as shown in Fig. 4(f). Si_x-SPAN shows promising commercial prospects for Li–S batteries, offering excellent electrochemical performance even under practical and harsh environments.[64–68] As shown in the comparative analyses in Tables S5–S7 (ESI†), the $Si_{0.05}$-SPAN electrode demonstrates exceptional rate capability, long-term cycling durability, and a high sulfur content.

To further assess the cycling performance, long-term cycling tests at 1.5 C are conducted, as shown in Fig. 4(g). The initial discharge capacities of $Si_{0.025}$-SPAN, $Si_{0.05}$-SPAN, $Si_{0.1}$-SPAN and SPAN are 737.4, 773.2, 723.6 and 391.5 mAh g^{-1}, respectively. The $Si_{0.05}$-SPAN electrode demonstrates the highest discharge capacity of 666.6 mAh g^{-1} after 500 cycles, with an ultralow decay rate of 0.028% per cycle, outperforming those in other reports (ESI, Table S5†). The coulombic efficiency of Si_x-SPAN remains stable at nearly 100% throughout the prolonged cycling process, ensuring the integrity of the discharge process. Moreover, with a sulfur loading of 5 mg cm^{-2} and an electrolyte/sulfur ratio of 10 μL mg^{-1}, the $Si_{0.05}$-SPAN electrode can deliver a high specific capacity of 817 mAh g^{-1} after 100 cycles (Fig. 4h), demonstrating excellent cycling performance at high sulfur loading in ether-based electrolytes.

To understand the origin of the enhanced electrochemical performance, we investigated the charge-transfer kinetics of the SPAN *vs.* Si-doped electrodes. Fig. 5(a) and S9† present the electrochemical impedance spectra (EIS) and the corresponding fitted equivalent circuits for different Si_x-SPAN composites. The intercept at high frequency corresponds to the ohmic resistance (R_{ohm}) of the cell, which represents the internal resistance of the electrode. The diameter of the semicircle in the mid-frequency range represents the charge-transfer resistance R_{ct} at the cathode/electrolyte interface. As seen in Fig. 5a, the $Si_{0.05}$-SPAN electrode exhibits a smaller semicircle compared to the undoped SPAN, indicating a lower R_{ct}. Quantitatively, fitting the spectra yields an R_{ohm} of ~5.6 Ω for SPAN, reduced to ~4.0 Ω for $Si_{0.05}$-SPAN, and an R_{ct} that drops from ~111.2 Ω (SPAN) to ~75.3 Ω ($Si_{0.05}$-SPAN). This reduction in charge-transfer resistance implies that the incorporation of SiQDs substantially improves the electrode's electrical connectivity and ionic access, likely through the combined effects of a more conductive matrix (due to higher graphitization and Si's intrinsic conductivity) and additional polar sites (Si–S bonds) that can facilitate interfacial charge transfer.[69,70] Fig. 5b compares the galvanostatic discharge–charge curves at 0.5 C for the different cathodes. The $Si_{0.05}$-SPAN cathode exhibits the smallest overpotential (difference between charge and discharge plateaus) of 0.6 V, which is consistent with faster kinetics and easier electrochemical reactions, reaffirming the beneficial role of Si–S bond formation in facilitating the redox processes. The effect of Si doping on redox kinetics is further evidenced by cyclic voltammetry at identical scan rates for the different electrodes (Fig. 5c). The $Si_{0.05}$-SPAN cathode exhibits a higher peak current density and improved redox reversibility (810 mV *vs.* 1030 mV), indicating accelerated redox kinetics due to SiQD incorporation. Fig. 5d presents the Tafel plots for both anodic and cathodic reactions. The Tafel slope for $Si_{0.05}$-SPAN is significantly smaller than those of other samples in both reactions, indicating that the reaction rate is less impeded by activation overpotentials, showing that the catalytic activity for polysulfide conversion is enhanced in the presence of SiQDs. These results collectively highlight that Si–S bond integration not only stabilizes sulfur but also endows the SPAN cathode with enhanced catalytic properties, likely by pro-

viding new active sites (Si sites bonded to sulfur) that can accelerate the lithium sulfide conversion reactions.[71,72] In essence, the SPAN framework doped with SiQDs behaves like a more effective electrocatalyst for the sulfur redox reactions, which is crucial for achieving high rates and long cycle life in Li–S batteries.[73,74]

We next probed lithium-ion diffusion kinetics in the electrodes using CV at various scan rates (Fig. 5e and f). According to the Randles–Sevick equation $\left(I_p = 2.69 \times 10^5 n^{\frac{3}{2}} A D_{Li^+}^{\frac{1}{2}} v^{\frac{1}{2}} \Delta C_{Li^+} \right)$, the peak current ($I_p$) in a diffusion-controlled redox process is proportional to the square root of the scan rate ($v^{1/2}$), with the proportionality constant related to the Li^+ diffusion coefficient (D_{Li^+}) in the electrode material.[75] By plotting I_p *versus* $v^{1/2}$ for the redox peaks, we can extract the relative Li^+ diffusion rates. Fig. 5g and h show the linear fits for the oxidation and reduction peaks of SPAN *vs.* $Si_{0.05}$-SPAN. From the slopes, we estimate that the apparent Li^+ diffusion coefficients in $Si_{0.05}$-SPAN are increased by approximately 8.1-fold ($D_{Li^+} = 1.73 \times 10^{-13}$ cm^2 s^{-1}, for the anodic process) and 4.7-fold ($D_{Li^+} = 3.35 \times 10^{-13}$ cm^2 s^{-1}, for the cathodic process) compared to pristine SPAN (2.14×10^{-14} and 7.16×10^{-14} cm^2 s^{-1}, respectively), demonstrating significantly enhanced Li^+ diffusion properties after Si coupling.[76,77]

To gain an atomic-level understanding of how Si doping influences the SPAN electronic structure and polysulfide binding, we performed DFT calculations. In particular, we examined the projected density of states (PDOS) and relative bonding energetics for Si in different configurations. The PDOS for the $Si_{0.05}$-SPAN model (with Si in a SPAN matrix) is shown in Fig. 5i–l. A strong overlap between carbon 2p and sulfur 2p is observed around the Fermi level (−3 to 3 eV), reflecting the covalent C–S interactions inherent to SPAN. When examining the contributions of silicon, we find that the overlap between Si 2p and C 2p (or Si 2p and N 2p) states is relatively minor and occurs mainly in the range above the Fermi level (around 1–3 eV), suggesting that Si does not strongly interact with the carbon or nitrogen of the PAN backbone. In contrast, there is a pronounced overlap between Si 2p and S 2p orbitals extending from ~0 to 6 eV (Fig. 5l), indicating a significant covalent interaction between Si and S. In other words, the electronic states of Si in the doped SPAN are hybridized with sulfur states much more than with carbon or nitrogen states. This supports the notion that Si preferentially bonds with sulfur atoms in the structure (forming Si–S bonds) and that these bonds are robust in an electronic sense (contributing states near the Fermi level, which can facilitate charge transfer).

We also evaluated the relative stability of possible Si bonding configurations *via* formation energy calculations (Fig. S10†). We modelled a local segment of the SPAN structure and placed a Si atom in different bonding environments: (i) bonded to a sulfur atom (forming a Si–S–C linkage), (ii) bonded to a nitrogen in the PAN ring (Si–N–C), and (iii) bonded to a carbon in the PAN backbone (Si–C–C). The calculated binding energies (or formation energies) reveal that the Si–S bonding configuration is the most favorable, with a for-
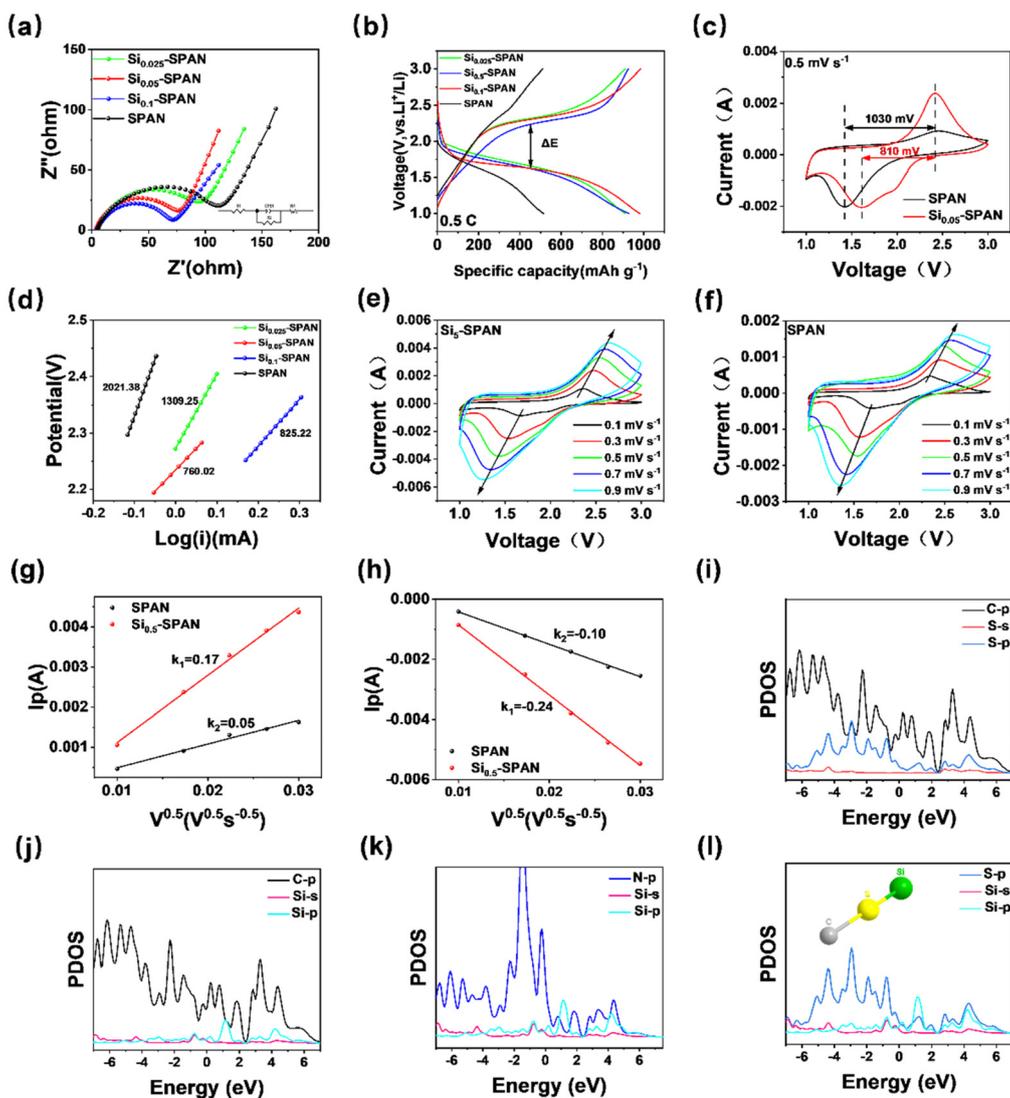
Fig. 5 (a) Nyquist plots of the SPAN and Si_x-SPAN cathodes. (b) Corresponding electrochemical discharge and charging curves at a current density of 0.5 C; (c) CV curves of $Si_{0.025}$-SPAN, $Si_{0.05}$-SPAN, $Si_{0.1}$-SPAN, and SPAN cathodes tested at 0.5 mV s^{-1}. (d) Tafel plots of the SPAN and Si_x-SPAN cathodes with different doping concentrations. (e) and (f) CV curves of the $Si_{0.05}$-SPAN and SPAN cathodes at various scan rates. (g) and (h) The linear relationship between the peak current and square root of scan rates measured at the oxidation and reduction peaks. The simulated PDOS for C, S (i) and Si (j) atoms. Si adsorption on N atoms (k) and S atoms (l).

mation energy of approximately −4.842 eV. In comparison, the Si–C configuration has a formation energy of −4.01 eV, and Si–N is much less favorable at −1.11 eV. The substantially larger magnitude of the Si–S bond energy corroborates the experimental inference that Si will preferentially react with and attach to sulfur (rather than to the carbon or nitrogen of the PAN matrix) during the high-temperature synthesis. These theoretical findings, together with the spectroscopic evidence, confirm that Si is chemically bonded to sulfur forming a network of Si–S bonds that is both energetically stable and electronically active.

To further elucidate the impact of Si–S bonds on charge distribution, we performed differential charge density analysis. Fig. 6a–c show the charge density difference maps for a model

system containing Si–S, Si–C, or Si–N bonds. In the Si–S bonded system (Fig. 6a), a significant accumulation of electron density (yellow regions) is observed around the sulfur atom, while a depletion of electron density (blue regions) is seen around the silicon. This indicates that electrons are partially transferred from Si to S when a Si–S bond is formed, consistent with sulfur being more electronegative. In contrast, the Si–C (Fig. 6b) and Si–N (Fig. 6c) systems show much less pronounced charge transfer between Si and the other element. These comparisons reinforce that Si–S bonds have a strong polar-covalent character that can localize electron density onto sulfur, lowering the energy barrier of the S conversion. A planar-averaged charge difference analysis (Fig. 6d–f) along the direction across the Si–S interface further highlights this
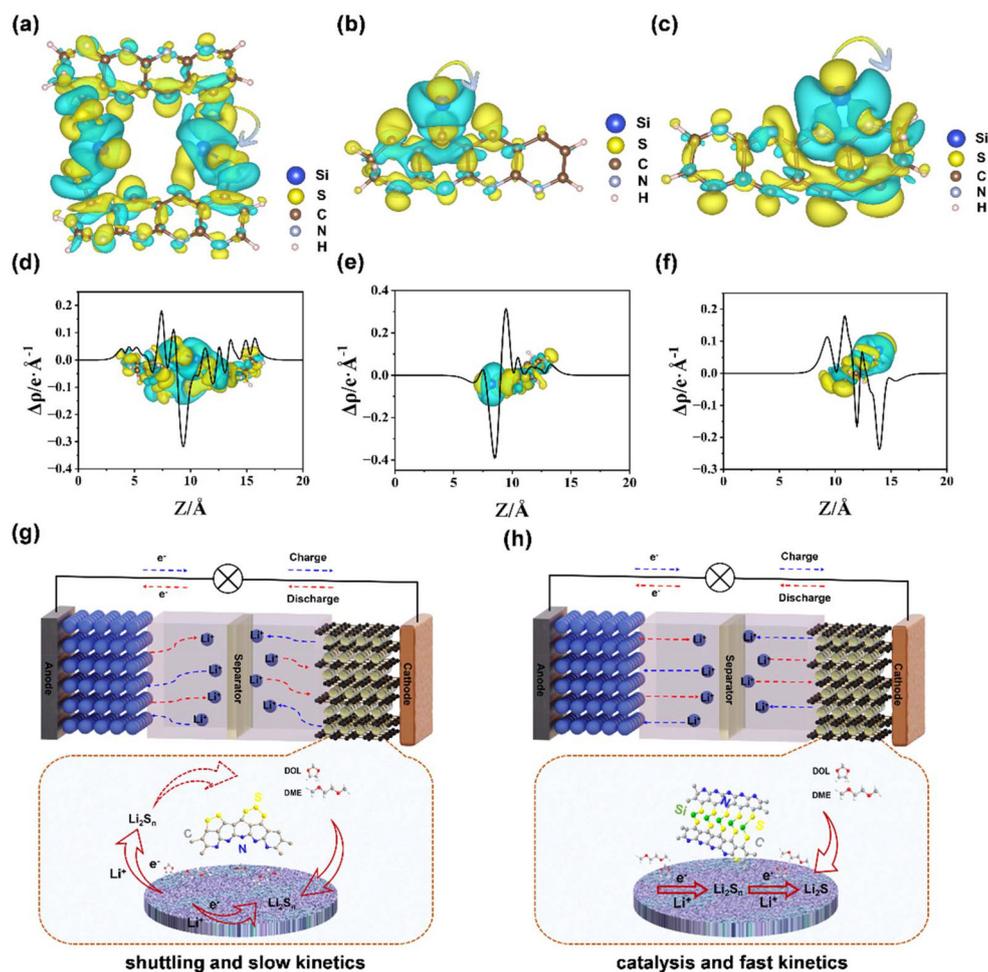
Fig. 6 Differential charge density map of Si–S, Si–C and Si–N (a–c, the arrow indicates charge transfer), and corresponding planar differential charge density maps (d–f). (g and h) The scheme of the proposed reaction process.

effect. A clear peak of negative charge appears on the S side of the bond, while a corresponding positive depletion is observed on the Si side (particularly around 9–10 Å in Fig. 6d). This net transfer of electron density from Si to S has important implications for the electrochemistry of the system. By increasing the electron density of sulfur atoms, the Si–S bonds can activate the sulfur, making it more nucleophilic and better able to engage in redox reactions with lithium.

In typical ether-based electrolytes, polysulfides dissolve and diffuse from the SPAN anode, resulting in rapid capacity decay.[78] However, the Si$_x$-SPAN cathode exhibits much slower capacity decay and reduced polarization voltage, suggesting accelerated redox transformation of polysulfide intermediates and enhanced reaction kinetics in ether-based electrolytes. The catalytic effect of Si doping significantly enhances the redox conversion of polysulfide and improves the reaction kinetics, leading to excellent electrochemical performance of the Li–Si$_x$-SPAN batteries, as shown in Fig. 6g. To further understand the benefits of Si doping, batteries after 500 cycles of charging and discharging are disassembled and analyzed.

Fig. S11† shows the structure of the disassembled cell along with TEM images of the electrode, revealing that the cathode structure remains tightly intact after prolonged cycling, with numerous carbon nanotubes intertwined with SPAN. High-angle annular dark-field scanning transmission electron microscopy (HAADF-TEM) and EDS images confirm the uniform distribution of C, N, S, and Si in the electrodes after cycling, further supporting the strong covalent interactions between Si and S that prevent the S species aggregation after 500 cycles. Elemental analysis (EA) (Table S8†) revealed that the sulfur content remained nearly unchanged and XPS (Fig. S13†) showed the retained Si–S binding configuration after 500 cycles, confirming the long-term effectiveness and structural stability of Si–S bonding in sulfur retention.

Moreover, we performed SEM characterization of the electrode and the separator (Fig. S12†). The electrode maintains its porous structure without rupture, with a significant amount of active material attached to the cavities and surface. Similarly, no significant damage is observed on the surface of the separator. Fig. S12(e) and (f)† compare the optical images

of Li metal after cycling in $Si_{0.05}$-SPAN and SPAN cells, showing darker Li metal (indicative of accumulated dead lithium and insulating deposits) in SPAN cells. The lighter color of the lithium in the $Si_{0.05}$-SPAN cell suggests that less polysulfide reached the anode and that the Li surface is smoother. The enhanced polysulfide stabilization is also supported by our UV-Vis spectroscopy of the disassembled cells (Fig. S14†), where a clear polysulfide signal is observed for the SPAN cathode, whereas no detectable signal appears for the $Si_{0.05}$-SPAN cathode. These observations confirm that Si–S bond engineering in the cathode leads to markedly improved electrode integrity and anode stability by suppressing the deleterious polysulfide shuttle and maintaining active material utilization over long cycles.

4. Conclusions

In summary, we have demonstrated for the first time that integrating covalent Si–S bonds into SPAN cathodes is an effective strategy to boost their sulfur content and electrochemical performance. The formation of robust Si–S bonds during high-temperature synthesis enables SPAN to retain a high active sulfur loading (37.93 wt% at 450 °C) while minimizing free sulfur, and simultaneously improves the electronic conductivity of the cathode. As a result, the $Si_{0.05}$-SPAN cathode (with only 5% SiQDs added) achieves a high discharge capacity of 1432.7 mAh g^{-1} at 0.1 C and exhibits an exceptionally long cycle life with low capacity fading even at high rates. This rational design provides a new pathway for the design of practical high-performance Li–S batteries, bridging the gap between fundamental materials innovation and real-world energy storage applications.

Conflicts of interest

There are no conflicts to declare.

Data availability

The data that support the findings of this study are available from the corresponding author upon reasonable request.

Acknowledgements

References

1 M. Armand and J. M. Tarascon, *Nature*, 2008, **4517179**, 652–657.

2 A. Eftekhari, *J. Mater. Chem. A*, 2018, **67**, 2866–2876.

3 S. Chu and A. Majumdar, *Nature*, 2012, **4887411**, 294–303.

4 Y. Chen, T. Wang, H. Tian, D. Su, Q. Zhang and G. Wang, *Adv. Mater.*, 2021, **33**, 2003666.

5 R. Deng, M. Wang, H. Yu, S. Luo, J. Li, F. Chu, B. Liu and F. Wu, *Energy Environ. Mater.*, 2022, **53**, 777–799.

6 Y. Huang, L. Lin, C. Zhang, L. Liu, Y. Li, Z. Qiao, J. Lin, Q. Wei, L. Wang, Q. Xie and D.-L. Peng, *Adv. Sci.*, 2022, **9**, 2106004.

7 R. Kumar, J. Liu, J.-Y. Hwang and Y.-K. Sun, *J. Mater. Chem. A*, 2018, **625**, 11582–11605.

8 B.-J. Lee, C. Zhao, J.-H. Yu, T.-H. Kang, H.-Y. Park, J. Kang, Y. Jung, X. Liu, T. Li, W. Xu, X.-B. Zuo, G.-L. Xu, K. Amine and J.-S. Yu, *Nat. Commun.*, 2022, **13**, 4629.

9 S. Li, D. Leng, W. Li, L. Qie, Z. Dong, Z. Cheng and Z. Fan, *Energy Storage Mater.*, 2020, **27**, 279–296.

10 J. Xie, B.-Q. Li, H.-J. Peng, Y.-W. Song, M. Zhao, X. Chen, Q. Zhang and J.-Q. Huang, *Adv. Mater.*, 2019, **3143**, 1903813.

11 J. Wang, J. Yang, J. Xie and N. Xu, *Adv. Mater.*, 2002, **1413–14**, 963–965.

12 X. Zhao, C. Wang, Z. Li, X. Hu, A. Abdul Razzaq and Z. Deng, *J. Mater. Chem. A*, 2021, **9**, 19282–19297.

13 H. Yang, C. Guo, J. Chen, A. Naveed, J. Yang, Y. Nuli and J. Wang, *Angew. Chem., Int. Ed.*, 2019, **583**, 791–795.

14 W. Zhang, S. Li, L. Wang, X. Wang and J. Xie, *Sustainable Energy Fuels*, 2020, **47**, 3588–3596.

15 K. Yu, G. Cai, M. Li, J. Wu, V. Gupta, D. J. Lee, J. Holoubek and Z. Chen, *ACS Appl. Mater. Interfaces*, 2023, **1537**, 43724–43731.

16 Z. Li, J. Zhang, Y. Lu and X. W. Lou, *Sci. Adv.*, 2018, **46**, eaat1687.

17 H. Raza, S. Bai, J. Cheng, S. Majumder, H. Zhu, Q. Liu, G. Zheng, X. Li and G. Chen, *Electrochem. Energy Rev.*, 2023, **61**, 29.

18 Z. Huang, P. Jaumaux, B. Sun, X. Guo, D. Zhou, D. Shanmukaraj, M. Armand, T. Rojo and G. Wang, *Electrochem. Energy Rev.*, 2023, **61**, 21.

19 B. He, Z. Rao, Z. Cheng, D. Liu, D. He, J. Chen, Z. Miao, L. Yuan, Z. Li and Y. Huang, *Adv. Energy Mater.*, 2021, **1114**, 2003690.

20 J. Guo, Z. Wen, Q. Wang, J. Jin and G. Ma, *J. Mater. Chem. A*, 2015, **339**, 19815–19821.

21 S. Ma, P. Zuo, H. Zhang, Z. Yu, C. Cui, M. He and G. Yin, *Chem. Commun.*, 2019, **5536**, 5267–5270.

22 S. Ma, Y. Wang, C. Fu, Y. Ma, Y. Gao, G. Yin and P. Zuo, *Chem. Commun.*, 2020, **5684**, 12797–12800.

23 A. R. Baboukani, I. Khakpour, E. Adelowo, V. Drozd, W. Shang and C. Wang, *Electrochim. Acta*, 2020, **345**, 136227.

24 A. Balakumar, A. B. Lysenko, C. Carcel, V. L. Malinovskii, D. T. Gryko, K.-H. Schweikart, R. S. Loewe, A. A. Yasseri,

Z. Liu, D. F. Bocian and J. S. Lindsey, *J. Org. Chem.*, 2004, **695**, 1435–1443.

25 M. Ashuri, Q. He and L. L. Shaw, *Nanoscale*, 2016, **81**, 74–103.

26 L. Zhao, S.-H. Han, S. Okada, B.-K. Na, K. Takeno and J.-i. Yamaki, *J. Power Sources*, 2012, **203**, 78–83.

27 C. Chatgilialoglu, *Chem. Rev.*, 1995, **955**, 1229–1251.

28 C. Chatgilialoglu, *Chem. – Eur. J.*, 2008, **148**, 2310–2320.

29 H. Chen, L. Wu, Y. Wan, L. Huang, N. Li, J. Chen and G. Lai, *Analyst*, 2019, **14413**, 4006–4012.

30 J. Shao, C. Huang, Q. Zhu, N. Sun, J. Zhang, R. Wang, Y. Chen and Z. Zhang, *Nanomaterials*, 2024, **1413**, 1155.

31 S. Wei, L. Ma, K. E. Hendrickson, Z. Tu and L. A. Archer, *J. Am. Chem. Soc.*, 2015, **13737**, 12143–12152.

32 C. Pan, Q. Wen, L. Ma, X. Qin and S. Feng, *New J. Chem.*, 2021, **4528**, 12528–12537.

33 X. Yu, J. Xie, Y. Li, H. Huang, C. Lai and K. Wang, *J. Power Sources*, 2005, **1461**, 335–339.

34 S. Al-Dallal, M. Hammam, S. M. Al-Alawi, S. Aljishi and A. Breitschwerdt, *Philos. Mag. B*, 1991, **634**, 839–848.

35 M. Hammam, *Mod. Phys. Lett. B*, 1992, **0608**, 469–475.

36 Y. Xu, Y. Yang, S. Lin and L. Xiao, *Anal. Chem.*, 2020, **9223**, 15632–15638.

37 N. Wei, M.-X. Wei, B.-H. Huang, X.-F. Guo and H. Wang, *Dyes Pigm.*, 2021, **184**, 108848.

38 C. F. J. Kuo, M. A. Weret, H. Y. Hung, M. C. Tsai, C. J. Huang, W. N. Su and B. J. Hwang, *J. Power Sources*, 2019, **412**, 670–676.

39 M. Frey, R. K. Zenn, S. Warneke, K. Müller, A. Hintennach, R. E. Dinnebier and M. R. Buchmeiser, *ACS Energy Lett.*, 2017, **23**, 595–604.

40 J.-S. Kim, T. H. Hwang, B. G. Kim, J. Min and J. W. Choi, *Adv. Funct. Mater.*, 2014, **2434**, 5359–5367.

41 M. Gerwig, M. Schwarz, E. Brendler and E. Kroke, *Eur. J. Inorg. Chem.*, 2016, **201628**, 4557–4560.

42 X. Dong, X. Fang, Y. Wang and X. Song, *Opt. Express*, 2018, **2618**, A796–A805.

43 X. Hu, H. Jiang, Q. Hou, M. Yu, X. Jiang, G. He and X. Li, *ACS Mater. Lett.*, 2023, **58**, 2047–2057.

44 M. A. Weret, C.-F. Jeffrey Kuo, T. S. Zeleke, T. T. Beyene, M.-C. Tsai, C.-J. Huang, G. B. Berhe, W.-N. Su and B.-J. Hwang, *Energy Storage Mater.*, 2020, **26**, 483–493.

45 K. Hirai, M. Tatsumisago, M. Takahashi and T. Minami, *J. Am. Ceram. Soc.*, 1996, **792**, 349–352.

46 T. Tsujimura, X. Xue, M. Kanzaki and M. J. Walter, *Geochim. Cosmochim. Acta*, 2004, **6824**, 5081–5101.

47 K. Kravitz, A. Kamyshny, A. Gedanken and S. Magdassi, *J. Solid State Chem.*, 2010, **1836**, 1442–1447.

48 R. A. Faulkner, J. A. DiVerdi, Y. Yang, T. Kobayashi and G. E. Maciel, *Materials*, 2013, **61**, 18–46.

49 Y. G. Kolyagin, V. N. Zakharov, A. V. Yatsenko and L. A. Aslanov, *Russ. Chem. Bull.*, 2015, **648**, 1829–1832.

50 P. Wang, X. Dai, P. Xu, S. Hu, X. Xiong, K. Zou, S. Guo, J. Sun, C. Zhang, Y. Liu, T. Zhou and Y. Chen, *eScience*, 2023, **31**, 100088.

51 H. Liu, F. Liu, Z. Qu, J. Chen, H. Liu, Y. Tan, J. Guo, Y. Yan, S. Zhao, X. Zhao, X. Nie, X. Ma, Z. Pei and M. Liu, *Nano Res. Energy*, 2023, **2**, e9120049.

52 A. P. Dementjev, A. de Graaf, M. C. M. van de Sanden, K. I. Maslakov, A. V. Naumkin and A. A. Serov, *Diamond Relat. Mater.*, 2000, **911**, 1904–1907.

53 J. L. Lou, H. W. Shiu, L. Y. Chang, C. P. Wu, Y.-L. Soo and C.-H. Chen, *Langmuir*, 2011, **277**, 3436–3441.

54 M. Hu, F. Liu and J. M. Buriak, *ACS Appl. Mater. Interfaces*, 2016, **817**, 11091–11099.

55 J. H. Oh, H. Um, Y. K. Park, M. Kim, D. Kim, E.-K. Bang, R. H. Kang and D. Kim, *Colloids Surf., B*, 2023, **222**, 113055.

56 A. Abdul Razzaq, Y. Yao, R. Shah, P. Qi, L. Miao, M. Chen, X. Zhao, Y. Peng and Z. Deng, *Energy Storage Mater.*, 2019, **16**, 194–202.

57 Y.-H. Lai, C.-T. Yeh, Y.-H. Lin and W.-H. Hung, *Surf. Sci.*, 2002, **5191**, 150–156.

58 A. Haas, *Angew. Chem., Int. Ed. Engl.*, 1965, **412**, 1014–1023.

59 Y.-H. Lai, C.-T. Yeh, C.-C. Yeh and W.-H. Hung, *J. Phys. Chem. B*, 2003, **10735**, 9351–9356.

60 W. E. Morgan and J. R. V. Wazer, *J. Phys. Chem.*, 1973, 77, 964–969.

61 R. Nordberg, H. Brecht, R. G. Albridge, A. Fahlman and J. R. Van Wazer, *Inorg. Chem.*, 1970, **911**, 2469–2474.

62 Y. Zhang, Y. Zhao, A. Yermukhambetova, Z. Bakenov and P. Chen, *J. Mater. Chem. A*, 2013, **12**, 295–301.

63 A. Mentbayeva, A. Belgibayeva, N. Umirov, Y. Zhang, I. Taniguchi, I. Kurmanbayeva and Z. Bakenov, *Electrochim. Acta*, 2016, **217**, 242–248.

64 H. Kim, J. Lee, H. Ahn, O. Kim and M. J. Park, *Nat. Commun.*, 2015, **61**, 7278.

65 Y.-J. Li, J.-M. Fan, M.-S. Zheng and Q.-F. Dong, *Energy Environ. Sci.*, 2016, **96**, 1998–2004.

66 H. Ye, L. Ma, Y. Zhou, L. Wang, N. Han, F. Zhao, J. Deng, T. Wu, Y. Li and J. Lu, *Proc. Natl. Acad. Sci. U. S. A.*, 2017, **11450**, 13091–13096.

67 G. Zhou, E. Paek, G. S. Hwang and A. Manthiram, *Nat. Commun.*, 2015, **61**, 7760.

68 L. Xu, H. Zhao, M. Sun, B. Huang, J. Wang, J. Xia, N. Li, D. Yin, M. Luo, F. Luo, Y. Du and C. Yan, *Angew. Chem., Int. Ed.*, 2019, **58**, 11491.

69 W. Hu, Y. Peng, Y. Wei and Y. Yang, *J. Phys. Chem. C*, 2023, **1279**, 4465–4495.

70 R. Qin, Z. Wang, J. Li and L. Deng, *J. Alloys Compd.*, 2022, **929**, 167355.

71 Z.-Q. Xu, R. Zou, W.-W. Liu, G.-L. Liu, Y.-S. Cui, Y.-X. Lei, Y.-W. Zheng, W.-J. Niu, Y.-Z. Wu, B.-N. Gu, M.-J. Liu, F. Ran and Y.-L. Chueh, *Chem. Eng. J.*, 2023, **471**, 144581.

72 Z.-L. Xu, S. Lin, N. Onofrio, L. Zhou, F. Shi, W. Lu, K. Kang, Q. Zhang and S. P. Lau, *Nat. Commun.*, 2018, **91**, 4164.

73 Y. Li, J. Wu, B. Zhang, W. Wang, G. Zhang, Z. W. Seh, N. Zhang, J. Sun, L. Huang, J. Jiang, J. Zhou and Y. Sun, *Energy Storage Mater.*, 2020, **30**, 250–259.

74 M. Wang, H. Yang, K. Shen, H. Xu, W. Wang, Z. Yang, L. Zhang, J. Chen, Y. Huang, M. Chen, D. Mitlin and X. Li, *Small Methods*, 2020, **49**, 2000353.

75 J.-Q. Huang, T.-Z. Zhuang, Q. Zhang, H.-J. Peng, C.-M. Chen and F. Wei, *ACS Nano*, 2015, **93**, 3002–3011.

76 S. Luo, C. Zheng, W. Sun, Y. Wang, J. Ke, Q. Guo, S. Liu, X. Hong, Y. Li and W. Xie, *Electrochim. Acta*, 2018, **289**, 94–103.

77 G. Zhou, H. Tian, Y. Jin, X. Tao, B. Liu, R. Zhang, Z. W. Seh, D. Zhuo, Y. Liu, J. Sun, J. Zhao, C. Zu, D. S. Wu, Q. Zhang and Y. Cui, *Proc. Natl. Acad. Sci. U. S. A.*, 2017, **1145**, 840–845.

78 X. Chen, L. Peng, L. Wang, J. Yang, Z. Hao, J. Xiang, K. Yuan, Y. Huang, B. Shan, L. Yuan and J. Xie, *Nat. Commun.*, 2019, **101**, 1021.